Compact angle-resolved metasurface spectrometer

Guiyi Cai[1, †], Yanhao Li[1 †], Yao Zhang[1], Xiong Jiang[1], Yimu Chen[1], Geyang Qu[2], Xudong Zhang[1], Shumin Xiao[1, 2, 3 #], Jiecai Han[3], Shaohua Yu[2 §], Yuri Kivshar[4,5 ¶], Qinghai Song[1, 2, 6 *]

1. Ministry of Industry and Information Technology Key Lab of Micro-Nano Optoelectronic Information System, Guangdong Provincial Key Laboratory of Semiconductor Optoelectronic Materials and Intelligent Photonic Systems, Harbin Institute of Technology, Shenzhen 518055, P. R. China.
2. Pengcheng Laboratory, Shenzhen 518055, P. R. China.
3. National Key Laboratory of Science and Technology on Advanced Composites in Special Environments, Harbin Institute of Technology, Harbin 150080, P. R. China.
4. Nonlinear Physics Center, Research School of Physics, Australian National University, Canberra ACT 2601, Australia.
5. Qingdao Innovation and Development Center, Harbin Engineering University, Qingdao 266000, China;
6. Collaborative Innovation Center of Extreme Optics, Shanxi University, Taiyuan 030006, Shanxi, P. R. China.

Corresponding authors:
shumin.xiao@hit.edu.cn; § yush@cae.cn;
¶ yuri.kivshar@anu.edu.au; * qinghai.song@hit.edu.cn

Abstract:

Light that scatters or radiates from a material carries valuable information about its origin. Angle-resolved spectroscopy became a key technique for uncovering such information, but it often requires a large optical apparatus, and thus its applications are hampered. Here, we suggest and demonstrate ultracompact angle-resolved spectral imaging by combining a tunable metasurface based miniature spectrometer array with a metalens. We show that high wavelength accuracy (~0.17 nm), high spectral resolution (~0.4 nm), and large linear dynamic range (~149 dB) can be well maintained even when the footprint of our spectrometer becomes as small as 4×4 μm2. We place an array of spectrometers directly at the back focal plane of metalens, achieving the angular resolution of 4.88×10^{-3} rad. Our angle-resolved spectrometers with metalenses may revolutionize the optical imaging and spectral analysis applications.

Main text

Light interacts with matter in a linear or nonlinear fashion as it travels through a medium. In principle, scattered or radiated light carries valuable information about the medium, e.g., surface roughness, defects, optical anisotropy, and optical nanostructures[1-3]. Being combined with a proper inverse problem model, the above information can be retrieved by measuring the light field at different angles and frequencies. Over the past two decades, angle-resolved spectral analysis has been intensively studied and successfully utilized to characterize performance of EUV mirrors [4], identify early-stage tumors [5, 6], and even determine the orientation of individual molecules [7, 8]. Despite their successes, conventional approaches (such as back focal plane imaging and stepwise sample rotation-based methods) often require submeter-scale optical setups and costly instrumentation[9-12]. High-performance and cost-effective angle-resolved spectrometers with ultra-compact form factors are still missing, thus strongly restricting the advent of many emerging applications such as devices for the Internet of Things, point-of-care diagnostics, and consumer electronics.

The main obstacle towards ultracompact angle-resolved spectrometer lies in the footprint of a single spectrometer. Commercial spectrometers offer high resolution but are too cumbersome for integrated systems. With the assistance of advanced nanophotonics and reconstruction algorithms, spectrometers have been successfully scaled down to submillimeter[13-15]or tens of micrometers [16-20]. Nevertheless, spectrometers with sufficient spectral resolution are still as large as 22×8 μm^2 [21]. To accommodate planar nanophotonics based angle-resolved imaging, the footprint of the spectrometer must be further reduced by more than an order of magnitude. In addition, the miniaturized spectrometers demonstrated so far are single devices[16-21]. CMOS-compatible technology and equipment cost for scaling up to spectrometer arrays are rarely considered [14,15,22,23]. Here, we employ the latest breakthroughs in nanophotonics and demonstrate the ultracompact angle-resolved meta-spectrometer.

Figure 1a depicts the sketch of our angle-resolved meta-spectrometer. It consists of metalens [24-28]and an array of spectrometers [13-23]. Metalens can transform incident light from distinct locations but at the same angle to a point on its back focal plane. The angle-dependent input signals (e.g., transmission, scattering, fluorescence, and Raman spectra of the analyte in real applications) are then converted to various patterns at the back focal plane. The position-dependent intensities and spectral contents of the patterns can be recorded by arrays of miniature spectrometers that simultaneously provide back-focal-plane images and angle-dependent spectra with reconstruction algorithm. The metalens and miniature spectrometer array replace traditional objective lens, imaging optical path, slit and spectrometer, enabling compression of sub-meter back focal plane imaging instruments[10, 11] to hundreds of microns.

Figure 1b illustrates the schematic and working principle of our miniature spectrometers in the array. Basically, light passing through a metasurface is modulated and then absorbed by a underneath photodetector [19, 29]. We use perovskite photodetectors as an example due to their ease of processing and compatibility with multiple ancillary materials, however, they can be replaced by other photodetectors (e.g., the currently commercialized CCD and CMOS) to

expand the applications of our concept. The photodetector signal is expressed as

$$S_i = \int I(\lambda)\, T_i(\lambda)\eta(\lambda)d\lambda,$$

where $I(\lambda)$, $T_i(\lambda)$, $\eta(\lambda)$ are the spectrum of the incident light, transmittance of the metasurface, and the spectral responsivity of the photodetector. Interactions between individual nanoparticles and periodic patterns endow metasurfaces with rich spectral features in $T_i(\lambda)$, e.g., sharp peaks and broadband background. Such spectral features correspond to distinct field distributions in the metasurface and respond individually to external perturbations, such as the surrounding refractive index (Fig. S2). By infiltrating liquid crystals [30] and applying an external voltage, one tunable metasurface is sufficient to produce a series of random $T_i(\lambda)$, equivalent to a metasurface array in conventional approaches[14, 15]. Then the spectral information of the incident light $I(\lambda)$ can be obtained from the measured S_i and $T_i(\lambda)$ using a reconstruction algorithm empowered by a neural network. Our improved reconstruction procedure (Fig. S1) reveals that eight $T_i(\lambda)$ of micron-scale metasurface are sufficient to produce spectra with high accuracy, high resolution, and high signal-to-noise ratio (Figs. 1c and 1d). As a result, the footprint of the spectrometer and the acquisition time (Fig. S3) can both be greatly saved.

Based on the above analysis, we have experimentally fabricated miniaturized spectrometers by combining electron beam lithography, reactive ion etching, and lift-off (Methods). A microscope image of one spectrometer (Fig. 2a) shows its in-plane active size is as small as 4×4 μm^2. Top-view scanning electron microscope (SEM) images show that the TiO_2 metasurface (Fig. 2b) is consistent with the design and the high film quality of perovskite is retained in such a small area (Fig. 2c). The metasurface infiltrated with liquid crystals and the perovskite photodetector are examined individually. The features in the transmission spectrum of the metasurface vary significantly with external voltage and thus form a basis for reconstruction (Fig. 2d). For the photodetector, we find its external quantum efficiency (EQE), responsivity (R), response time, and linear dynamic range are the same as large-area perovskite photodetectors (i.e., not affected by the tunable metasurface after integration) (Figs. S4, S5, S6). For the area of 4×4 μm^2, a particularly good device repeatability has also been experimentally confirmed (Fig. S7).

Then the photodetector and the tunable metasurface are packaged to form a miniaturized spectrometer, and its reconstruction performance is characterized (Methods). A broadband white light source passing through a bandpass filter is illuminated on our spectrometer after being measured by a commercial spectrometer. Eight photocurrents $S_{1\text{-}8}$ are achieved by increasing the external voltage (V_{LC}) applied on the tunable metasurface from 0 to 9 V. With the assistance of calibrated $T_{1\text{-}8}(\lambda)$, a broadband spectrum is thus reconstructed and plotted as the blue line in the bottom panel Fig. 2f and Fig. S8. The overall reconstruction agrees well with the reference spectrum recorded by a commercial spectrometer (orange line) in a wide spectral range from 400 nm to 700 nm. Similarly, we have also verified the ability of our spectrometer to construct narrow-linewidth spectra. As depicted in the top panel of Fig. 2f, the narrow peaks positioned between 440 nm and 660 nm have been well reconstructed and are consistent with the reference spectra.

To explore the spectral resolution, we illuminate the spectrometer with a high-density monochromatic light of wavelengths from ~525 to 535 nm and reconstruct all the spectra (Fig. 2g). It is obvious that our spectrometer can resolve the monochromatic light with high accuracy. The wavelength difference ($\Delta\lambda$) between reconstructed and reference spectra varies between 0.04 nm and 0.30 nm, with an average value of ~0.17 nm (bottom panel of Fig. 2h). The average wavelength resolving power ($R_\lambda=\lambda/\Delta\lambda$) of our spectrometer is also as high as 3200 (top panel of Fig. 2h). Then the high spectral resolution of our spectrometer is tested with a Mercury-vapor lamp. The double yellow lines at ~576.96 nm and 579.07 nm can be well resolved (Fig. 2i). All these performances are close to or even better than the state-of-the-art miniaturized spectrometer [21], even though our device area is more than an order of magnitude smaller.

Beyond the sparse spectrum, we have also challenged the capability of our spectrometer in to reconstruct dense and mixed spectra. Figure 3a shows the top-view SEM image of a perovskite-based microdisk with radius R ~ 13.7 nm that supports lasing of whispering gallery modes (WGMs) (Fig. S9). The microdisk is excited by a frequency-doubled Ti: Sapphire laser (400 nm, 100 fs pulse width, 1kHz repetition rate) and the emissions are recorded by a commercial spectrometer and our spectrometer, respectively. The experimental results are shown as blue and orange lines in Fig. 3b. Both the broad photoluminescence peak and the high-density periodic WGM peaks have been well resolved by our 4×4 μm^2 spectrometer and match the reference spectrum very well (Fig. S10). The free spectral range (FSR) in Fig. 3b is around 1.2 nm and the full width at half maximum is only 0.9 nm. Thus, we know that our spectrometer has the ability to resolve complicated spectra in a broad spectral range. The resolution limit of our spectrometer is examined with a larger perovskite microdisk with R = 90.99 μm. Inset in Fig. 3d reveals that two peaks with 0.4 nm wavelength difference has been clearly resolved.

In addition to the wavelength, the relative intensities of emission spectra can also be resolved by considering the absolute values of photocurrents. One example is depicted in Fig. 3c, where the emissions from the perovskite microdisk laser at different pumping fluences are recorded and reconstructed. At low pumping power, the spectrum is a broadband photoluminescence centered around 530 nm. With the increase of excitation, the broad photoluminescence peak increases slightly and narrow peaks emerge at ~ 550 nm and increase dramatically. The intensities of WGM peaks are much stronger than the photoluminescence when pumping fluence is 1.35 $\mu J/cm^2$. By integrating the intensity within spectral range from 545 nm to 558 nm, we have plotted the output intensity as a function of pumping fluence (Fig. 3d). A "S"-shaped curve can be clearly seen in the log-log plot, indicating the onset of perovskite microlasers. All these observations are consistent with the previous reports [31] and reference spectra (Fig. S10) well. Interestingly, some fine features, such as band-filling induced blueshift of microlasers, have also been resolved. Our results demonstrate the capability of our miniaturized spectrometer for real applications of high-quality spectral analysis.

The spectral analysis performance of our spectrometers, combined with a CMOS-compatible fabrication process, facilitates scaling from a single spectrometer to spectrometer arrays, which is ideal for hyperspectral imaging. We have fabricated a spectrometer array and tested their performance in spectral imaging. The microscope image in Fig. 4a shows the spectrometer

array and its readout circuits. The entire spectrometer array occupies an area of ~50×50 μm^2 and is composed of 10×10 individual spectrometers. The SEM images (insets in Fig. 4a) show detailed information of internal metasurfaces and photodetectors. All the structural parameters are identical to the single spectrometer in Fig. 2a picture of a cartoon lion is defined on a screen and projected onto the spectrometer array with an optical lens (Fig. 4a). Photocurrent measurements at each spectrometer are recorded and reconstructed to a spectral data cube (x, y, λ). Cross sections of the cube relate to the images of the photograph at individual wavelengths (Fig. 4b). By integrating the spectral cube along λ, a pseudo-colour image (Fig. 4c) and spectral measurements (Fig. 4d) are achieved and almost identical to the results of optical measurements (Fig. S11). Thus, the spectrometer array can function more than a spectral imaging camera and characterize the position-dependent spectral information.

The advances in ultrasmall spectrometers and spectrometers array naturally lead to the emergence of compact angle-resolved spectrometers. In our research, it is realized by placing the spectrometer array to the back focal plane of a metalens (Fig. 5a). The metalens is designed and fabricated in a 1200 nm Si_3N_4 membrane on a K9 glass substrate (300 μm). It has a diameter of 600 μm (Fig. 5b) to fit the camera of a cellphone and is insensitive to the polarization of incident light due to its square-shaped pixels (inset in Fig. 5b). The corresponding optical characterizations reveal that the metalens can focus the incident plane wave to a diffraction-limited spot at the distance of 800 μm away from it (Fig. 5c and Fig. S12). Such a long focal length leaves both the focal point and back focal plane in the air and enables the direct integration of metalens and spectrometer array.

Then the performance of our angle-resolved spectrometer is tested with a TiO_2 grating at its focal point (Figs. S13, S14). A white light source passing a bandpass filter is focused onto the sample. The transmitted beams along different directions (θ, ϕ, λ) are collected by the metalens and converted to different spots at the back focal plane (x, y, λ). Such spots are then captured by the spectrometer array and become photocurrents with location information (x, y). Like the above spectral imaging, the spectral data cube (x, y, λ) can be reconstructed with the trained neural networks and eventually corresponds to the angle-dependent data cube (θ, ϕ, λ). By selecting different angles (ϕ), the angle-dependent spectrum at (θ, 0, λ) and (θ, π/2, λ) are plotted in Figs. 5d and 5e. The dashed lines correspond to the numerical results. We can see that our device can clearly resolve the angle-dependent spectra and match the numerical designs well. The spectral details and the anisotropy of grating are well reconstructed. The integration of spectral information can also give the back focal plane image (Fig. 5f). It is also consistent with the conventional back focal plane image (Fig. S15) but with detailed information at each wavelength (Figs. 5g-5i, Fig. S15). The experimentally demonstrated angle resolution is 4.88×10^{-3} rad, comparable to the commercial angle-resolved spectrometer[9]. The size of the entire system is only 0.226 mm^3, suitable for many emerging applications such as in vivo diagnostics and consumer electronics.

In summary, we have combined the recent breakthroughs in nanophotonic devices with the reconstruction algorithms and successfully scaled the footprint of the spectrometer down to 4×4 μm^2. Owing to the advances in device size and nanofabrication technology, we have

extended the spectrometer concept to meta-array devices and directly integrated it with a metalens. As a result, we have demonstrated, for the first time to our knowledge, an ultracompact angle-resolved spectrometer with record-small size, high spectral resolution, and high angular resolution. Our angle-resolved spectrometer can be further improved by developing a sub-micrometer spectrometer or combining it with a metalens array [32, 33]. This research shall bring a new paradigm to optical imaging, point-of-care detection, and wearable optoelectronics etc.

Methods

Numerical simulation. The unit cells of metasurfaces are numerically designed with a commercial software of finite element method (COMSOL Multiphysics). Each unit cell has an all-dielectric nanostructure with C4 rotational symmetry surrounded by air or liquid crystals. The refractive index of dielectrics such as TiO_2, Si_3N_4, and liquid crystals are directly taken from the experimentally measured results. Periodic boundary conditions are applied in x-y directions to accurately determine the wavelength dependent phases and transmissions of transmitted waves. In the propagating direction, perfect matching layers are applied to fully absorb the outgoing waves and mimic the infinite large propagating distance.

Device fabrication. Metasurfaces are fabricated with a combined process of electron beam (E-beam) lithography and reactive ion etching. 800 nm TiO_2 film is deposited onto a ITO coated glass substrate using E-beam evaporation (SKE_A_75). Next, a 100 nm layer of polymethyl methacrylate (PMMA A2) electron-beam resist is spin-coated onto the sample and baked at 180 °C for 1 hour. The Raith E-line electron-beam writer is utilized to create a pre-designed pattern on the resist. After developing with the MIBK & IPA (1:3) solution, 25 nm Cr layer is deposited onto the sample with E-beam evaporation followed by a lift-off process. Taking the remaining Cr patterns as a mask, a reactive ion etching (RIE) process (Oxford Plasma System 100) is employed to transfer the nanostructures into TiO_2 film. The TiO_2 metasurface is achieved after removing Cr mask in a Cr etchant solution (Aldrich Chemistry).

We develop a fully top-down etching-based technology for Si_3N_4 metalens. 910 nm Si_3N_4 layer is deposited on a K9 glass substrate (300 μm) by the PECVD. Then 35 nm Cr layer is deposited by the electron beam evaporation and further coated with 60 nm PMMA A2 resist. The E-beam resist is patterned in Raith E-line and developed as the above. 20 nm SiO_2 layer is deposited onto the PMMA nanostructures via E-beam evaporation, followed by a lift-off process. Taking the SiO_2 as a mask, the nanostructures are transferred to the Cr layer and then the Si_3N_4 etching. The metalens is obtained after the removal of Cr mask as the above.

Perovskite photodetectors are fabricated using ITO-coated mica plates as the transparent electrode. The thickness of ITO film is 135 nm. Then SnO_2 film is spin-coated onto the substrate and annealed at 150 ^oC for 30 min. The $MAPbI_3$ perovskite precursor (1.3 M) is prepared by solving MAI, Pb, and I (molar ratio of 1:1:2) in a mixture of DMF: DMSO with a volume ratio of 4:1. The substrate is first spinning at 1,000 r.p.m. for 10 s, and then at 5000 r.p.m. for 30 s. At 5 s of the second stage, 300 μl chlorobenzene antisolvent is dropped on top of the spinning substrates. The perovskite film is achieved after annealing at 100°C for 10 min. Then 200 nm ZEP520A E-beam resist is spin-coated onto the film and an array of square roles

are opened by E-beam lithography. A thin layer of Spiro-OMeTAD is spin-coated on the perovskite film as the hole transport layer, followed by E-beam evaporation of Au electrodes.

2μm liquid crystal cell is realized by controlling the thickness with polystyrene (PS) microspheres. The liquid crystal box is sealed in three directions, and one side is open. Then drop a drop of liquid crystal on the open side, and put the whole sample into a vacuum box. After repeated pumping and deflation for 3-5 times, the liquid crystal can completely fill the liquid crystal cell. The sample is ready for characterization after sealing the open side.

Optical characterization. The optical setups are clearly shown in figures of the main text. The incident light is collimated to a uniform beam by an optical lens. After passing a filter or a monochromator (Zolix Omni-λ300 monichromator), the beam with specific spectral information is focused by an objective lens to the meta-spectrometer or a commercial spectrometer (Princeton Instruments IsoPlane SCT320). The spectral information is thus achieved via reconstruction algorithm and compared with the reference ones obtained with the commercial spectrometer. By inserting the image to a LED screen, the pattern is imaged by an optical lens onto the behind meta-spectrometer array, and then the (x, y, λ) information of projector photo is obtained via spectrum reconstruction.

The angle-resolved spectroscopy is recorded by combining the meta-spectrometer array with a Si_3N_4 metalens. The analyte is placed at the focal point of metalens and illuminated by a collimated beam. The diffracted light is collected by the metalens and distributed to angle-dependent pattern at its back focal plane, where the meta-spectrometer array is positioned. Both back focal plane image and angle-dependent spectrum are obtained via spectrum reconstruction.

In the lasing experiment, a frequency doubled femtosecond laser (400 nm, 1kHz repetition rate, 100 fs pulse width) is focused onto one perovskite microdisk by an objective lens. The emission from the microdisk is collected by an optical lens at the side and coupled to the meta-spectrometer or a commercial spectrometer.

Spectrum reconstruction. We use a compressed sensing algorithm based on neural networks to reconstruct the spectrum. The neural network is composed of two sections. The first section is a single-layer linear fully connected layer with $N_V \times N_\lambda$ matrix weights, consisting of the transmittance spectrum T and the spectral response η of the detector. These weights, denoted as W_T, are fixed during the network training process. The input datasets of the network contain 100k random spectra, each spectrum is composed of M Gaussian distributions with random means, variances, and amplitudes

$$I = \sum_{i=1}^{M} \exp(-\frac{(\lambda - \lambda_i)^2}{2\sigma_i^2}) .$$

The output of the first part of the network is proportional to the photocurrent value measured by the spectrometer at different voltages in the following expression

$$S = W_T I = T(\lambda)\eta(\lambda) I .$$

The second part of the network is a fully connected network with a LeakyReLU nonlinear activation layer including 6 layers, denoted F, so the output of the network is:

$$O = F\{S\} = F\{T(\lambda)\eta(\lambda)I\}.$$

The Loss function of the network uses mean square error (MSE) between the reconstructed spectrum O of the output and the input spectrum I, and uses the Adam optimizer with default parameters for gradient descent:

$$MSE = \frac{1}{N_\lambda}\sum_{n=1}^{N_\lambda}(O(\lambda_n) - I(\lambda_n))^2.$$

In the test process, the first part of the network is no longer enabled. The current measured by the detector is fed directly into the second part of the network, resulting in the final reconstructed spectrum. We use peak signal to noise ratio (PSNR) to calibrate the effectiveness of reconstruction:

$$PSNR = 10\log_{10}(\frac{\max(O(\lambda))^2}{MSE}).$$

The training and testing processes were completed by Python v3.9.0 and PyTorch v1.12.1 (Facebook Inc.) on a personal computer equipped with an NVIDIA RTX 3090 graphical processing unit, Intel Core i9 CPU, and 128 GB of RAM. It usually took 4 hours for a typical training of the entire process.

References:

1. Wax, A., Yang, C., Dasari, R. R. & Feld, M. S. Measurement of angular distributions by use of low-coherence interferometry for light-scattering spectroscopy. *Opt. Lett.* **26**, 322–324 (2001).
2. Schröder, S., Herffurth, T., Blaschke, H. & Duparré, A. Angle-resolved scattering: an effective method for characterizing thin-film coatings. Appl. Opt. 50, C164–C171 (2011).
3. Ling, X. *et al.* Anisotropic Electron-Photon and Electron-Phonon Interactions in Black Phosphorus. *Nano Lett.* **16**, 2260–2267 (2016).
4. Trost, M., Schröder, S., Feigl, T., Duparré, A. & Tünnermann, A. Influence of the substrate finish and thin film roughness on the optical performance of Mo/Si multilayers. *Appl. Opt.* **50**, C148–C153 (2011).
5. Kim, Y. L. *et al.* Simultaneous measurement of angular and spectral properties of light scattering for characterization of tissue microarchitecture and its alteration in early precancer. *IEEE J. Sel. Top. Quantum Electron.* **9**, 243–256 (2003).
6. Roy, H. K. *et al.* Four-dimensional elastic light-scattering fingerprints as preneoplastic markers in the rat model of colon carcinogenesis. *Gastroenterology* **126**, 1071–1081 (2004).
7. Lieb, M. A., Zavislan, J. M. & Novotny, L. Single-molecule orientations determined by direct emission pattern imaging. *J. Opt. Soc. Am. B* **21**, 1210-1215 (2004).
8. Hänisch, C., Lenk, S. & Reineke, S. Refined Setup for Angle-Resolved Photoluminescence Spectroscopy of Thin Films. *Phys. Rev. Appl.* **14**, 064036 (2020).
9. http://www.ideaoptics.com
10. Wagner, R., Heerklotz, L., Kortenbruck, N. & Cichos, F. Back focal plane imaging spectroscopy of photonic crystals. *Appl. Phys. Lett.* **101**, 081904 (2012).

11. Zhang, X., Liu, Y., Han, J., Kivshar, Y. & Song, Q. Chiral emission from resonant metasurfaces. *Science* **377**, 1215–1218 (2022).
12. Chen, Y. *et al.* Observation of intrinsic chiral bound states in the continuum. *Nature* **613**, 474–478 (2023).
13. Yang, Z., Albrow-Owen, T., Cai, W. & Hasan, T. Miniaturization of optical spectrometers. *Science* **371**, (2021).
14. Wang, Z. *et al.* Single-shot on-chip spectral sensors based on photonic crystal slabs. *Nat. Commun.* **10**, 1–6 (2019).
15. Tittl, A. *et al.* Imaging-based molecular barcoding with pixelated dielectric metasurfaces. *Science* **360**, 1105–1109 (2018).
16. Bao, J. & Bawendi, M. G. A colloidal quantum dot spectrometer. *Nature* **523**, 67–70 (2015).
17. Yang, Z. *et al.* Single-nanowire spectrometers. *Science* **365**, 1017–1020 (2019).
18. Yuan, S., Naveh, D., Watanabe, K., Taniguchi, T. & Xia, F. A wavelength-scale black phosphorus spectrometer. *Nat. Photonics* **15**, 601–607 (2021).
19. Guo, L. *et al.* A Single-Dot Perovskite Spectrometer. *Adv. Mater.* **34**, 2200221 (2022).
20. Meng, J., Cadusch, J. J. & Crozier, K. B. Detector-Only Spectrometer Based on Structurally Colored Silicon Nanowires and a Reconstruction Algorithm. *Nano Lett.* **20**, 320–328 (2020).
21. Yoon, H. H. *et al.* Miniaturized spectrometers with a tunable van der Waals junction. *Science* **378**, 296–299 (2022).
22. Yesilkoy, F. *et al.* Ultrasensitive hyperspectral imaging and biodetection enabled by dielectric metasurfaces. *Nat. Photon.* **13**, 390-396 (2019).
23. Xiong, J. *et al.* Dynamic brain spectrum acquired by a real-time ultraspectral imaging chip with reconfigurable metasurfaces. *Optica* **9**, 461-468 (2022).
24. Kildishev, A. V., Boltasseva, A. & Shalaev, V. M. Planar Photonics with Metasurfaces. *Science* **339**, 1232009–1232009 (2013).
25. Khorasaninejad, M. *et al.* Metalenses at visible wavelengths: Diffraction-limited focusing and subwavelength resolution imaging. *Science* **352**, 1190–1194 (2016).
26. Wang, S. *et al.* A broadband achromatic metalens in the visible. *Nat. Nanotechnol.* **13**, 227–232 (2018).
27. Chen, W. T. *et al.* A broadband achromatic metalens for focusing and imaging in the visible. *Nat. Nanotechnol.* **13**, 220–226 (2018).
28. Santiago-Cruz, T. *et al.* Resonant metasurfaces for generating complex quantum states. *Science* **377**, 991–995 (2022).
29. García de Arquer, F. P., Armin, A., Meredith, P. & Sargent, E. H. Solution-processed semiconductors for next-generation photodetectors. *Nat. Rev. Mater.* **2**, 1–17 (2017).
30. Li, S.-Q. *et al.* Phase-only transmissive spatial light modulator based on tunable dielectric metasurface. *Science* **364**, 1087–1090 (2019).
31. Tang, H. *et al.* Ultrahigh-Q Lead Halide Perovskite Microlasers. *Nano Lett.* **23**, 3418–3425 (2023).
32. Li, L. *et al.* Metalens-array–based high-dimensional and multiphoton quantum source. *Science* **368**, 1487–1490 (2020).
33. Lin, R. J. *et al.* Achromatic metalens array for full-colour light-field imaging. *Nat. Nanotechnol.* **14**, 227–231 (2019).

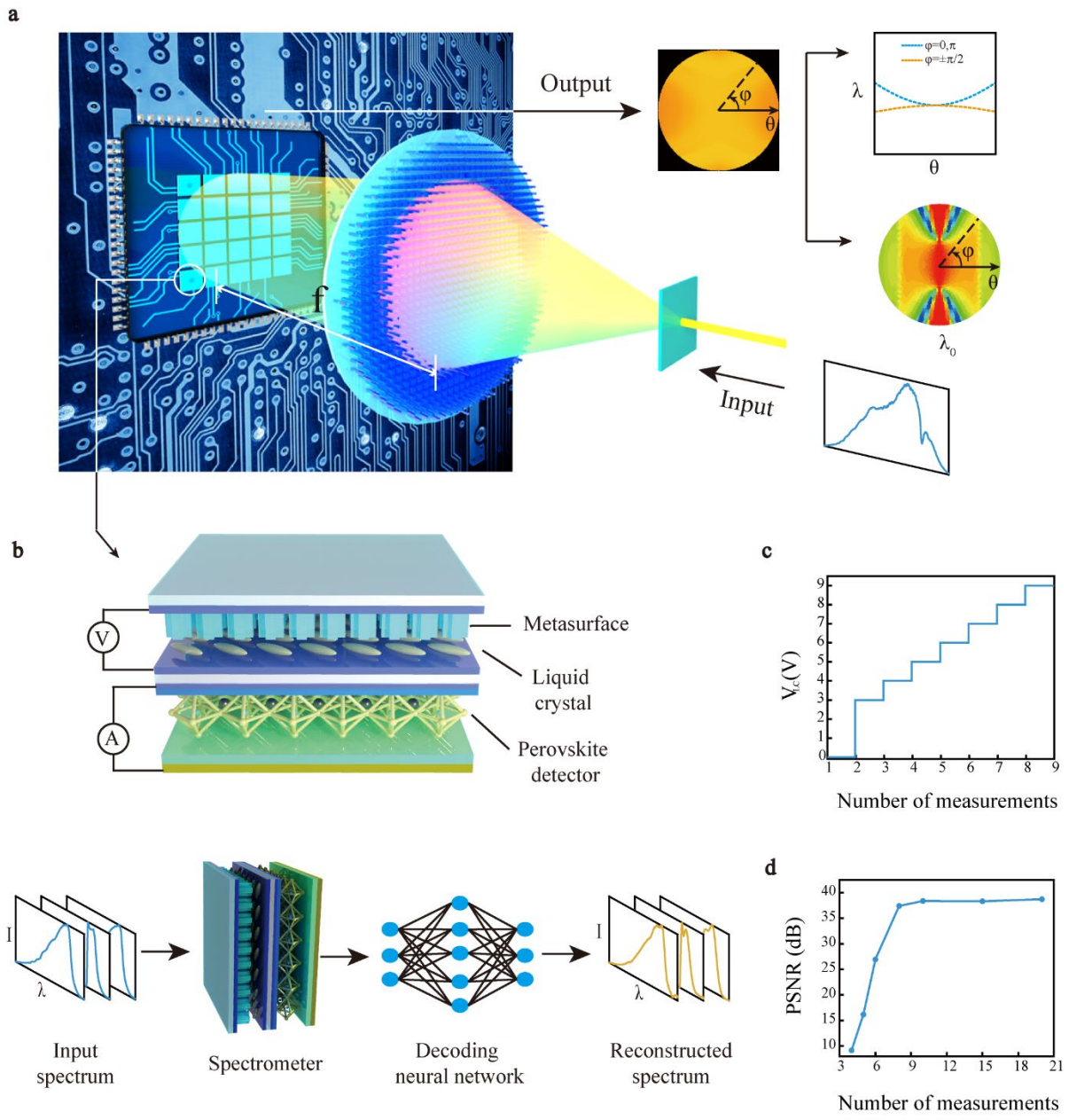

Figure 1. Design principles for angle-resolved metasurface spectrometers. (**a**) Schematic of angle-resolved spectral analysis. (**b**) Schematic and operation flow of a single ultracompact meta-spectrometer and the reconstructed spectrum. (**c**) Input voltage steps for multiple measurements. (**d**) Dependence of signal to noise ratio of reconstructed spectrum on the number of $T_i(\lambda)$.

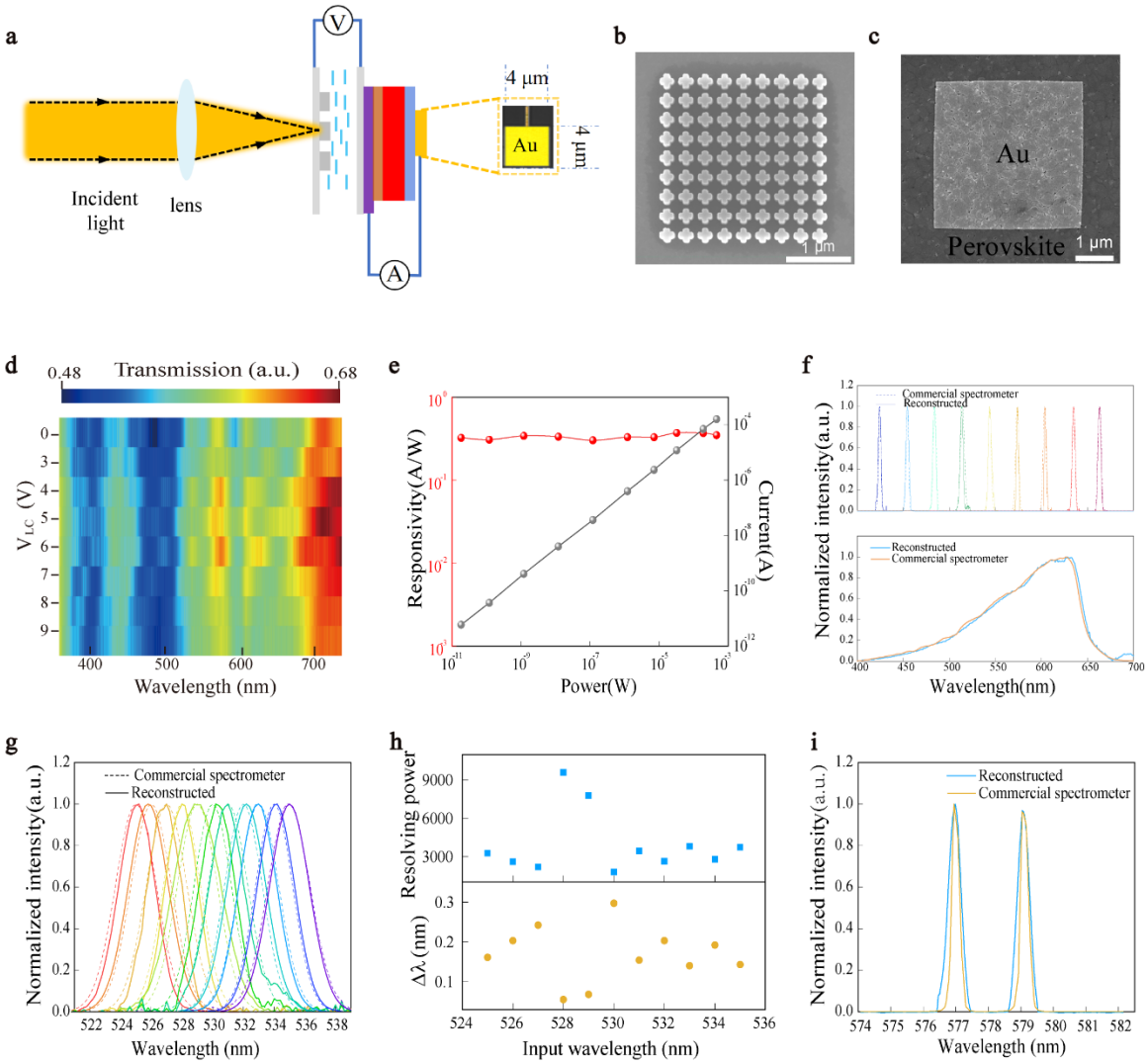

Figure 2. Demonstration of ultracompact metasurface spectrometer. (**a**) Schematics of optical setup and ultracompact meta-spectrometer. Inset shows the optical microscope image of the spectrometer. (**b**) and (**c**) are the top-view SEM images of Si metasurface and Au electrode on perovskite film within the spectrometer. (**d**) Experimentally recorded transmission spectra of liquid crystal infiltrated metasurface with different external voltages. (**e**) Responsivity(R) and linear dynamic range (LDR) of the perovskite photodetector with an area of 4×4 μm^2. (**f**) Reconstructed spectra of broad (bottom) and narrow (top) band incident beams. The corresponding reference spectra recorded by a commercial spectrometer are shown as orange lines. (**g**) Monochromatic spectra constructed by our spectrometer (blue lines) and its reference spectra (orange lines). (**h**) Peak wavelength difference between reconstructed and reference spectra in G (bottom) and the wavelength resolving power of our spectrometer (top). (**i**) Reconstructed and reference spectra of double yellow lines of a mercury lamp.

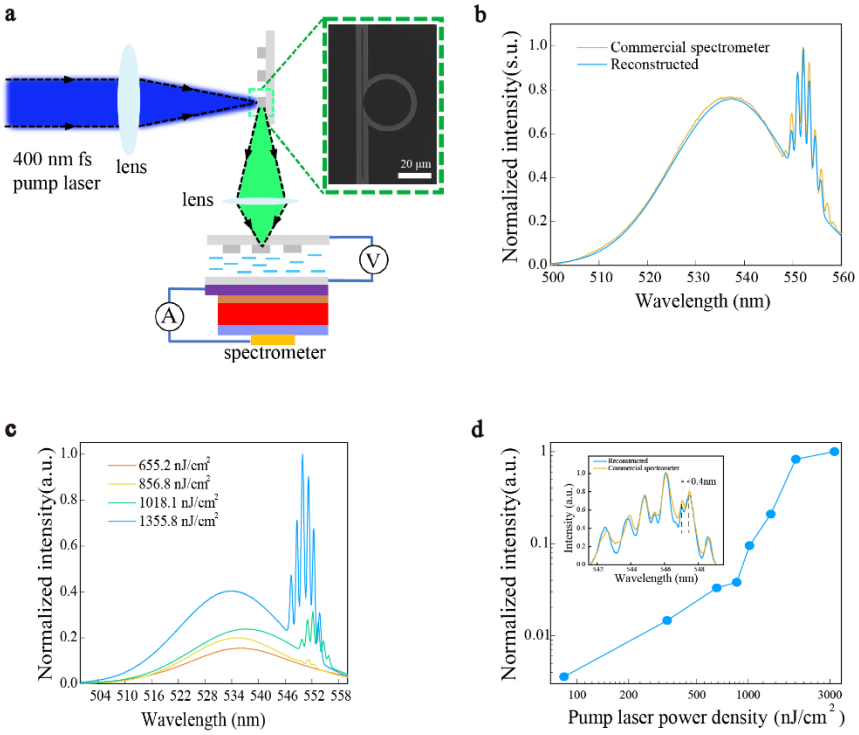

Figure 3. Characterization of microlasers with ultracompact metasurface spectrometer. (**a**) Schematic of optical setup for laser characterization. Inset shows top-view SEM image of perovskite microdisk. (**b**) Comparison between the computationally reconstructed spectrum (blue line) and the recorded spectrum with a commercial spectrometer (orange line). (**c**) Reconstructed emission spectra under different excitation fluence. (**d**) Integrated intensity of reconstructed spectra as a function of pumping fluence. Inset shows the reconstructed and reference spectra recorded from a perovskite microdisk with R = 90.99 μm. Two peaks with 0.4 nm difference can be resolved.

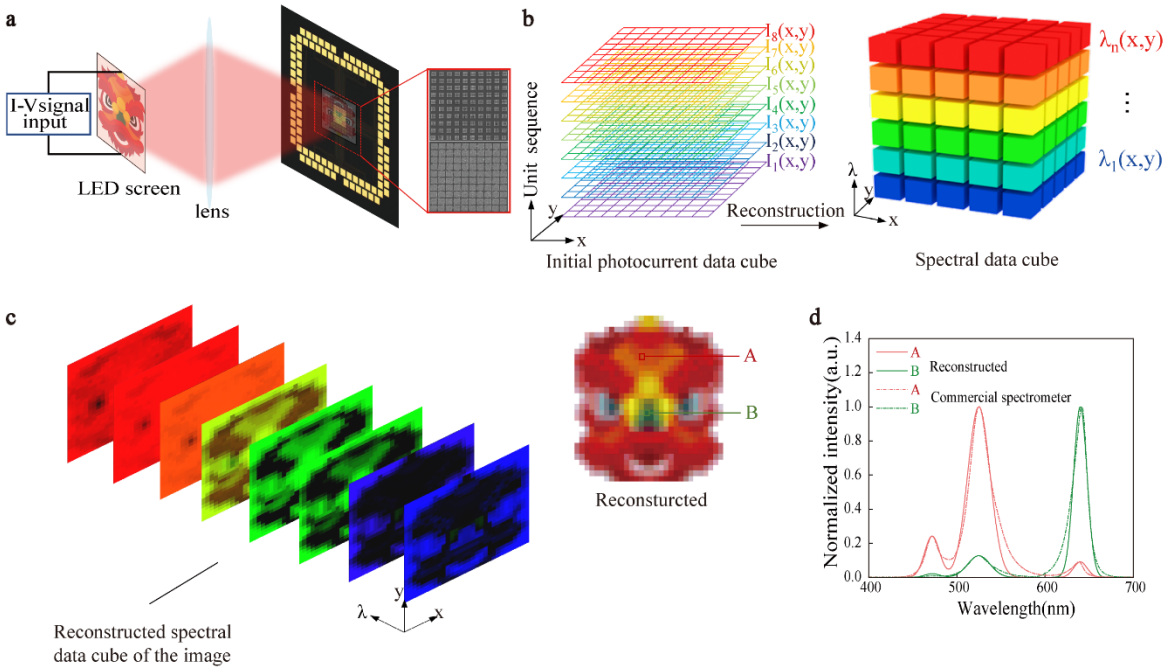

Figure 4. Array of metasurface spectrometers for spectral imaging. (**a**) Microscope image of meta-spectrometer array. Insets show the SEM images of the 10×10 TiO_2 metasurfaces and perovskite photodetectors. (**b**) Initial photocurrent data cube and the reconstructed spectral data cube. (**c**) Reconstructed images at different wavelengths. Inset shows the pseudo-color image converted from the spectra and the CIE color functions. (**d**) Reconstructed spectra at points A-B marked in (c). Dashed lines are reference spectra measured by a commercial spectrometer.

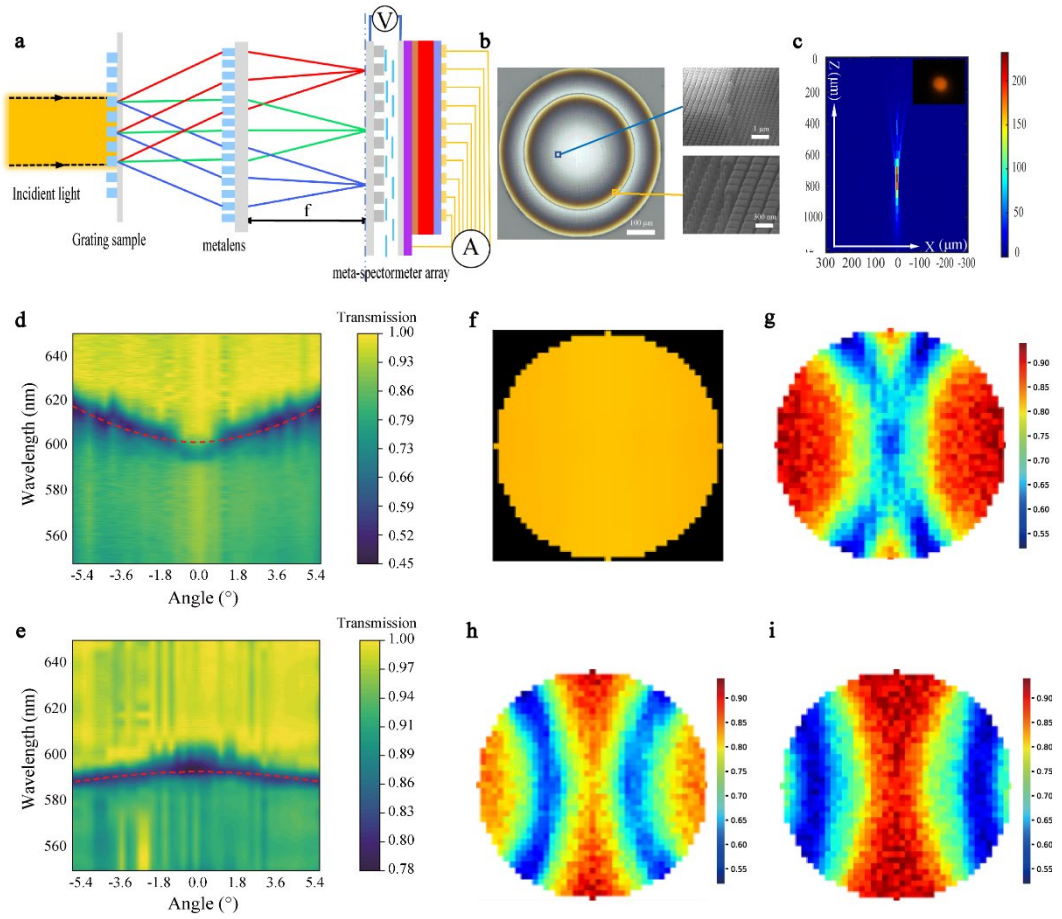

Figure 5. Angle-resolved spectral analysis and imaging. (**a**) Sketch of the angle-resolved meta-spectrometer. An array of miniaturized spectrometers is placed at the back focal plane of a Si_3N_4 metalens. A TiO_2 grating is positioned at the focal point and illuminated with a broadband light source. (**b**) Microscope image of Si_3N_4 metalens. The inset shows the high-resolution SEM image of the internal pixels. (**c**) Intensity distribution of light in x-y plane and y-z plane after passing through the metalens. (**d**) and (**e**) are the angle resolved spectra along (θ, $0/\pi$, λ) and (θ, $\pm\pi/2$, λ). The dashed lines represent the numerically calculated resonant wavelengths. (**f**) Pseudo-color back focal plane image of a TiO_2 grating constructed from the angle-resolved spectra and CIE color functions. (**g**)-(**i**) Back focal plane images of TiO_2 grating at 597 nm, 605 nm, and 611 nm.